E

MICHIGAN STATE
UNIVERSITY

National Superconducting Cyclotron Laboratory

STOPPING ENERGETIC HEAVY IONS IN ONE-BAR HELIUM: BROAD INCIDENT MOMENTUM DISTRIBUTIONS

In press: Nuclear Instruments and Methods

L. WEISSMAN, D.A. DAVIES, P.A. LOFY, and D.J. MORRISSEY

MSUCL-1284 **MAY 2004**

Stopping energetic heavy-ions in one-bar helium: broad incident momentum distributions.

L. Weissman*, D.A. Davies, P.A. Lofy and D.J. Morrissey.

National Superconducting Cyclotron Laboratory and Dept. of Chemistry, Michigan State University, East Lansing, MI-48824

(Dated: April 29, 2004)

Abstract

Various tests for stopping energetic ^{32}P fragments in a 50 cm gas cell filled with helium were performed. The fraction of ions stopped in the gas was measured as a function of the width of the incident beam momentum distribution. The use of a shaped degrader placed in a dispersive plane before the gas cell significantly improves the stopping efficiency in gas. A stopping efficiency of 35% was obtained for fragments with the broadest momentum distribution, which was an improvement of approximately 80%. Qualitative agreement between the experimental results and stopping power calculations was obtained.

PACS numbers: 24.10.Lx, 34.50.Bw

Keywords: stopping ions, gas-cell, stopping range, wedge degrader, range bunching

* corresponding author: weissman@nscl.msu.edu

I. INTRODUCTION

The collection of fast secondary beams after thermalization in a buffer gas will allow a new range of experiments to be performed with the most exotic beams. Therefore, the development and implementation of a so-called gas stopper is an important element of existing and planned fragmentation facilities. The stopping and collection of fast ions (E/A $\geq$ 100 MeV/u) available from projectile fragmentation reactions has the additional difficulty that the range straggling increases with increasing incident energy and the broad momentum distribution of the fragments [1, 2].

In a previous publication [3], the results of numerous tests for stopping various nearly monoenergetic (100-150 MeV/u) ions in helium were reported. The fraction of ions stopped in a 50 cm long gas cell was measured as a function of thickness of energy degrader, gas pressure and path length in helium. To obtain good agreement with the stopping power calculations, the small adjustment of only one parameter, the magnetic rigidity of the beam, was required. All other parameters in the calculations were fixed at the best known values. The tests demonstrated that a typical stopping efficiency higher than 50% can be achieved at a gas pressure of 1 bar. These tests were performed either with primary beams, that have a narrow beam momentum spread $\frac{\Delta P}{P}$=0.07%, or with secondary beams where the momentum distribution (0.2%< $\frac{\Delta P}{P}$ <0.5%) was cut by narrow momentum slits placed in the dispersive plane of the A1900 separator[4]. The total momentum spread of typical projectile fragment beams is determined by differential energy loss and energy straggling in the production target, the achromatic wedge used for beam purification, and by the reaction mechanism itself. A larger momentum acceptance of a fragment separator (5.5% in the case of the A1900) allows efficient collection of the momentum spread of fragmentation beams and, hence, maximizes the yields of exotic fragments. On the other hand, the large momentum spread of the beam before the slowing down process would result in a large range distribution and, consequently, a drastic reduction of the stopping efficiency in a gas cell with a realistic areal density. The gas has very small effective thickness, less than 10 mg/cm^2 in the case of the NSCL gas cell at 1 bar pressure. The problem can be overcome in part if the last stage of the slowing down process includes an ion-optical dispersive plane where the geometrical position of an ion depends on its energy as described by H. Weick et al. [1]. A specially shaped, monoenergetic, degrader can be placed in the dispersive plane just before the gas cell in order to compensate for the energy spread of a geometrically dispersed beam by larger (smaller) energy losses. This range compensation technique has been tested recently at the FRS separator [5] using standard ionization chambers.

We report on measurements made with a dedicated system under development that will provide a broad range of thermalized ions from the A1900 projectile fragment separator. The results include the first tests of stopping energetic secondary beams with broad momentum distributions and, demonstrate the proposed energy bunching method.

II. EXPERIMENT.

Fully-stripped primary beams of ^{36}Ar ions at 150 MeV/u beam energy were delivered from the coupled K500 and K1200 cyclotrons to the target position of the A1900 separator where a beryllium production target with 487 mg/cm^2 nominal thickness was placed. A 450 mg/cm^2 thick aluminum achromatic degrader was placed in the dispersive central plane (Image 2) of the separator. The curvature of the degrader corresponded to the effective

wedge angle of -0.88 mrad. The shape of the degrader resulted in achromatic trajectories of the fragments in the remaining part of the separator and allowed purification of the fragments of interest by using narrow slits placed in the A1900 focal plane. A thin ($\approx$ 30 mg/cm^2) plastic scintillator was placed in the center of the device (Image 2) for monitoring the beam intensity. Slits placed in the next dispersive plane of the A1900 after the achromatic wedge (Image 3) allowed variation of the final incident momentum distribution of the beam. The dispersion at Image 3 is 30 mm per percent in momentum, e. g. a 30 mm gap between the momentum slits allows 1% momentum spread of the beam at the exit of the A1900 separator.

The separator was tuned for transport and purification of ^{32}P fragmentation products. The choice of ^{32}P was primarily dictated by its high-production yield. The magnetic rigidity, $B\rho$, of the beam after passing the achromatic wedge and the thin scintillator was 3.359 T·m. The beam consists mostly of ^{32}P and some ^{33}S fragments with an almost negligible admixture of ^{31}Si (Table I).

The beam of the fragments was delivered to the gas stopping station described in detail in a previous publication [3]. A schematic diagram of the experimental setup is shown in Fig. 1. The optics of the beam line was tuned to produce a dispersive image in the horizontal plane at position A and an approximately parallel beam into the gas cell. The dispersion value at position A was measured and found to be 9.5 mm per percent of beam momentum spread.

The energy of ^{32}P fragments was degraded by a set of borosilicate glass (BSL7) plates that could be tilted in the horizontal plane. A computer controlled drive held a pair of 1.488 mm thick optically polished plates (90 mm horizontal $\times$ 30 mm vertical). The plates were rotated in opposite directions by a mechanical drive providing a smooth increase in thickness of the absorbing material that cancels, to first order, the effect of the small angular divergence of the beam. The conservative uncertainty in the degrader angle was estimated to be 0.25 degree, which should be combined with the uncertainty in the thickness of the plates ($\leq$2.5 μm). A ladder, placed at the point A, in Fig. 1, contained three positions with a phosphor screen, used for observation of the beam spot, a monochromatic wedge degrader (M-wedge) and a homogeneous degrader (H-wedge). The monoenergetic and homogeneous wedges were manufactured from 2024 alloy of aluminum using precision electric discharge machining. The area of the degraders was 60$\times$38 mm, and the wedge angle was along the longer side. The thicknesses of the wedges were measured with a digital micrometer. The typical local imperfection of the wedge surfaces was found to be less than 5 micrometers. The H-wedge was found to be 2.281(3) mm thick with global wedging angle less than 0.25 mrad. Thickness in the middle of the M-wedge was 2.241(6) mm and the wedge's angle was 10.8(2) mrad. The value of the wedge angle provides energy loss compensation as determined by the value of the horizontal dispersion at the point A, and, the beam energy and energy loss of the ^{32}P ions in aluminum [5]. The density of the wedge material was measured and found to be 2.759(1) g/cm^3 and its chemical composition was taken from the literature. The $B\rho$ for the two last quadrupole elements (see Fig. 1) was set to 2.030 T·m to account for the average energy loss in the degraders. A large Si PIN-detector (50mm$\times$50mm$\times$0.5mm) can be introduced in the beam at position B in Fig. 1 upstream from the gas cell during beam transport. The beam passed through a beryllium window into the gas cell filled with helium. The thickness of the window and diameter were 1.50 mm and 5.32 cm respectively. The thickness and diameter of the beryllium window were chosen so that deflection under the load from the helium gas would not cause a significant change in effective thickness across

its diameter.

A telescope consisting of two surface barrier detectors of 300 mm^2 active area and 0.1, 1.5 mm thick, respectively, was mounted on a central post inside the gas cell and was used for detection and identification of particles. The telescope was placed at the distance of 45(0.2) cm from the beryllium window. The relatively small area of the used detectors was dictated by the geometry of the electrodes placed inside the gas cell for extraction of the stopped fragments [6]. The Si telescope allowed identification of the ^{32}P fragments and contaminants that have a similar magnetic rigidity and cannot be completely separated by the A1900, as well as, from the lighter reaction products produced by interaction of the fragments in the degraders and the window. The time difference measured between a reference signal from the cyclotron and the fragment detection (time-of-flight) allowed for additional particle identification. Typical particle identification plots are shown in Fig. 2. As it can be seen from Fig. 2, the ^{32}P fragments were well separated from the main contaminants in the ΔE-TOF diagram down to the detector threshold. The signals were recorded on an event-by-event basis and energy histograms were obtained in off-line analysis.

Energy spectra observed in the detectors without the degrader or with thin degraders and with an evacuated gas cell consisted of sharp ΔE peaks. Comparison of positions of the ΔE peaks with the predictions of the stopping power calculations yielded the energy calibration. As the energy calibration relies on the stopping power calculations, its typical uncertainty is about 5% [7].

The low-energy threshold of the first detector was approximately 3 MeV. Thus, transmitted ions with lower energies were not registered. The under-threshold fraction can be calculated and corrected to first order by using spectra obtained from stopping power calculations [3]. This correction is significant (up to 10%) only for the largest glass degrader thickness and since the transmission fraction for these degrader angles is small, the applied correction does not significantly change the shape of transmission profiles.

The data were taken for various sets of parameters such as the type of wedge, the tilting angle of the glass degraders, gas pressure and value of the momentum acceptance. The momentum slits were set to 10, 30 and 60 mm, that corresponded to the 0.3%, 1 % and 2% incident momentum spread at the exit of the A1900. The optical setting of the beam line used to transport the secondary ions to the gas cell and produce a dispersion on the wedges introduced a correlation between angle and dispersion that limited the range of momenta that reached the detector in the gas. The reduced effective momentum acceptance is discussed below.

Numerous short, 1-2 minutes, measurements were performed. For example, after setting the gap of the momentum slits and gas pressure in the cell, the counting rate in the telescope was measured separately for the M- and H-wedges as a function of the tilting angle of the glass degraders. Thus, the transmission (number-distance) curves were obtained for the two wedges. The whole sequence of the measurements was repeated then for different values of the gap of the momentum slits. Then the entire series of measurements was repeated with an evacuated gas cell. For each measurement, the number of detected ^{32}P fragments was integrated using the identification plots (Fig. 2). All of the experimental results presented below have been corrected for fluctuations of the beam intensity as monitored by the plastic scintillator at the Image 2, and for the small fraction of events below the threshold.

III. RESULTS

A summary of the measurements is presented in Fig. 3 where the normalized transmission profiles, e.g. the dependence of the counting rate as a function of the glass degrader effective thickness for three values of the incident momentum distribution are represented by squares (M-wedge) and triangles (H-wedge). Open symbols correspond to the data for the evacuated chamber and filled symbols for the measurements taken at a helium pressure of 825 Torr. The vertical error bars are the combined statistical errors for measurements in the upstream plastic detector and the first detector of the telescope plus the error on the low-threshold correction (taken conservatively as 50 % of the added value for the narrow momentum distribution). As the stopping power calculations were found to be less reliable for the cases of broad momentum distributions (see below), the corresponding error on the low-threshold correction was taken as 100%. The horizontal error bars are due to uncertainties in the determination of the degrader angle plus absolute thickness uncertainty. The drop in the counting rate with increasing degrader thickness for the case of the evacuated chamber is due to the increasing fraction of ions stopped in the beryllium window. As expected, when helium is present, additional stopping of ions in helium results in an earlier drop in the counting rate with increasing degrader thickness. The transmission profiles were fitted with a simple function:

$$y = \frac{a}{1 + \exp\left(-(x-b)/k\right)}$$

The results of a least-square fitting procedure are shown in Fig. 3 as solid curves and the numerical results are contained in Table II. The table shows that the mid-point of the falling curve (b parameter) for the M-wedge is systematically larger than the corresponding value for the H-wedge. This difference, b^M-b^H, ranges from 74 micrometers for narrow momentum distribution, to 104 micrometers for the largest momentum distribution. Part of this difference ($\approx 40\mu$m) is due to a slightly thinner M-wedge compared to the H-wedge. The thickness of the M-wedge varies in the horizontal direction, therefore, the optimum thickness of the glass degrader depends on the relative positioning of the beam on the M-wedge. The larger b^M can be explained by a few mm shift of the beam spot with respect to the middle of the M-wedge.

The difference between transmission profiles with and without helium corresponds to the fraction of ions stopped in gas as a function of the degrader angle (stopping profile). The stopping profiles obtained by subtracting the fitted transmission functions are shown in Fig. 3 by dotted lines. The stopping profiles in turn were fitted by standard gaussian functions in order to obtain the stopping efficiencies:

$$y = y_c \exp - \frac{(x-x_c)^2}{2w^2}$$

where x_c is the thickness of the degrader that corresponds to the maximum stopped fraction, y_c the value of the maximum stopped fraction (maximum stopping efficiency) and w is the standard deviation of the stopping profiles. For each stopping profile, the conservative errors on the x_c, y_c and w parameters were obtained by taking limiting values of the b and k parameters from the fitting of the corresponding transmission profiles. The results of the fittings process are presented in Table III.

As seen in Fig. 3 and Table III, the stopping profiles for the M-wedge are considerably different from the corresponding profiles for the H-wedge. The former profiles are narrower

and have higher maximum stopping efficiencies, y_c, than the latter ones. In the case of the broadest momentum spread, the optimum stopping efficiency, y_c, obtained for the M-wedge is almost 80% higher and the corresponding width of the profile, w, is more than 60% smaller, indicating that the use of the monoenergetic degrader resulted in considerable energy compression. The effects of the smaller effective thickness of the M-wedge is also seen in the x_c^M-x_c^H values (Table III). It is also worth noting that the areas under the normalized stopping profiles, S, are the same for the two wedges (Table III) within the experimental error.

Although the Si detectors register ions after the Be-window and gas, e.g. after large energy straggling, rather than directly after the wedges, the energy bunching effect can also be seen in the residual energy spectra (the energy registered in the ΔE- and E- detectors were summed with the corresponding calibration coefficients). The residual energy spectra taken on an event-by-event basis for the H- and M-wedges, collected for different values of the momentum spread, are compared in Fig. 4a-b. The spectra were gated by the ^{32}P group using ΔE-TOF plots. The spectra presented in Fig. 4 were taken for zero angle of the glass degrader and the evacuated gas cell. Examining the residual spectra, one can observe the strong bunching effect for the case of the M-wedge. One also can observe that for both wedges, the behavior of the energy distribution is not consistent with the symmetric setting of the momentum slits as low-energy counts are added to the spectra as the momentum slits gap is widened. This effect indicates that ions from the high-energy part of the momentum distribution were not detected in the telescope. When the PIN detector (2500 mm^2 active area) is introduced in the beam the ratio of counting rates in the PIN and in the telescope (300 mm^2 active area) is constant as a function of the momentum slits gaps in the both Image 2 and Image 3 dispersive images, indicating good centering of the beam. However, retraction of both glass and wedge degraders resulted in increased counting rate in the telescope with respect to the PIN detector and the Image 2 plastic detector by a factor of ≈ 2. The beam optics that produces the dispersion at the wedge position is more sensitive to angle than to momentum. Small misalignment of the beam in the transport system can introduce an angle-momentum correlation that would easily deflect part of the secondary beam, resulting in a cut of the measured effective momentum spread. The beam spot is larger than the size of the telescope in the gas cell and, unfortunately, the present geometry of the gas cell does not allow introduction of larger area detectors in the cell that might avoid such ambiguities. The energy spectra can be qualitatively reproduced by calculations (see below) if effective momentum distributions and magnetic rigidities are introduced.

IV. STOPPING POWER CALCULATIONS

The experimental results for primary beams with narrow incident momentum distribution were reproduced well by stopping power calculations by slightly adjusting just one parameter, the beam magnetic rigidity [3]. However, the case of secondary beam is more complicated due to additional uncertainties associated with the wedge and beam transport. For example, a shift of beam position with respect to a center of a wedge degrader results in a shift in transmission and stopping profiles. Similarly, angle and momentum correlations generated in the beam line used to create the dispersion at the wedge may introduce an effective cut and shift in the momentum distributions measured in a small area detector. The measured residual energy and stopping power profiles were used to determine the effective beam momentum distribution and magnetic rigidities. The effective thickness of the

M-wedge was slightly adjusted due to uncertainty in the position of the beam on the wedge surface.

The stopping power calculations were performed with the LISE code [8] that simulates all magneto-optical elements used for beam transport from the cyclotron to the gas cell and includes all slits and materials used for beam degradation. Many parameters in the calculations, such as thicknesses of all degraders (except the M-wedge), their physical, chemical and geometrical properties and their geometrical position along the beam line, and the value of dispersion at the point A, were fixed to the best known values. Some of the beam optics parameters like the magnification and angular divergence of the beam were not known experimentally, and only the values calculated from a beam optic transport code were used. To simulate the effective cut in the measured beam momentum distribution, the gap of the Image 3 momentum slits and the beam rigidity were adjusted in calculations for each value of the nominal beam momentum spread. Both the obtained experimental stopping profiles and the residual energy spectra were used to adjust the latter parameters. The experimental stopping profiles are more suitable for adjusting the effective beam rigidity, as the calibration of the energy spectra has significant uncertainty. The comparison with experimental residual energy spectra was useful for obtaining the effective momentum distributions. The ATIMA model [9] integrated into the LISE code was used for stopping power calculations. The obtained effective parameters for the H-wedge data are listed in Table I.

As the next step, the thickness in the middle of the M-wedge was slightly adjusted to compensate the small offset of the beam position with respect to the wedge center. Good agreement between the calculations and the experiment corresponds to a 2.210 mm thick M-wedge or $\approx$ 3 mm shift with respect to the wedge center. The calculated residual energy spectra and stopping profiles are compared with experimental data in Fig 4 and Fig 5 respectively. One can observe that the qualitative agreement between the result of calculations and experiment is achieved. The effect of energy bunching for the M-wedge is clearly seen in the calculations. Thus, the calculation can be used in the future for design of shaped degraders.

V. DISCUSSION AND CONCLUSION.

Tests for stopping fragmentation beams with variable incident momentum distributions were performed. The energy bunching method using a shaped degrader for a geometrically dispersed beam was demonstrated. For the case of $\frac{\Delta P}{P}$=2% nominal momentum spread, the stopping efficiency of 35% in 45 cm of helium gas was achieved. This value is larger by a factor 80% than the corresponding efficiency obtained without the energy compression. As the stopping efficiencies were measured for the 45 cm length of helium and the total length of the gas cell is 50 cm, one can presume that the stopping efficiencies for the cell in first order are 10% higher than the y_c values in Table III. The measured momentum spread is reduced by a factor of 1.6 for the case of the broadest momentum distribution. The small area of the Si detectors makes the measurements very sensitive to the fine details of beam optics, and qualitative agreement between the calculations and the experiment was achieved only after introduction of an assumption regarding the beam transport.

It is interesting to compare the experimental results with the theoretical limit of the monoenergetic degrader performance. Following the discussion in [5, 10], one can estimate the limit of fragment velocity spread that can be obtained with a monoenergetic degrader

used in an ion-optic system:

$$\sigma_\nu^2 = (\frac{MW_\nu}{D})^2\sigma_x^2 + \sigma_{\delta\nu}^2$$

The first term corresponds to the optical resolving power of the system, with M and D the dispersion and magnification at the wedge position correspondingly ($M/D \approx 10^{-2}$ m for our system), σ_x is the beam size at the entrance of the ion-optic system and W_ν is defined by the beam velocities and the stopping powers in front and behind of the wedge degrader:

$$W_\nu = \frac{\beta_1^2\gamma_1(\frac{dE}{dx})_1}{\beta_2^2\gamma_2(\frac{dE}{dx})_2}$$

The second term, $\sigma_{\delta\nu}$, is the standard deviation of the velocity straggling due to the degrader. The contribution of the resolving power term for the ^{32}P fragments is 0.3 % spread per mm of the beam spot at the entrance to the system. Both LISE and Mocadi [11] calculations show that the velocity spread of a monoenergetic ^{32}P beam due to energy straggling in the glass, wedge, and the Be window is on the order of 3%. Thus, the limit of the final momentum distribution is determined mostly by energy straggling rather than by the optical resolution of the system. The smallest σ_ν corresponds to a stopping profile with a standard deviation, w, of approximately 0.019 mm glass degrader equivalent. This approaches the values obtained for the narrowest momentum distribution (see Table III). In the case of an ideal monoenergetic degrader, the final momentum distribution should not depend on the initial momentum spread of the beam [5, 10]. This is not the case for the experimental results (Fig 3 and Table III). One of the possible reasons for the non-ideal behavior is the wedge geometry. The desirable thickness tolerance for the degraders is on the level of a few 10^{-4} [5]. In the present experiment, at much lower beam energy and, hence, much thinner degraders in comparison with [5], the thickness tolerance was at least an order of magnitude poorer resulting in a reduction of the bunching efficiency. The experiments with heavier ions require thinner wedges and increased demands on the wedge accuracy. A larger value of momentum dispersion produced at the wedge plane will relax significantly demands on wedge accuracy.

The angle-momentum correlations introduced in the dispersion plane by degraders combined with further energy straggling during passage through the Be window may also be responsible for non ideal bunching behavior.

The successful implementation of the energy bunching method is important in the context of the recently proposed RIA facility [12] where a gas stopper will be used as a key element of the fragmentation based ISOL facility. The present and previous [3] work demonstrate the feasibility of efficient stopping of energetic fragmentation beams in one bar helium. However, efficient extraction of the stopped ions from the gas cell still has to be demonstrated. The first results of our extraction tests were briefly reported in [6]. Continued work on the first tests for extraction of stopped and thermalized radioactive ions will be addressed in a future report.

We would like to thank Mr. J. Ottarson for his help with design and fabrication of the experimental setup and the staff the NSCL laboratory for their help during the experiments and Dr. O. Tarasov for his help in use of the LISE code. This work is support by the National Science Foundation grant PHY-01-10523 and by the US Department of Energy grant 00ER41144.

[1] H. Weick *et al.*, Nucl. Instr. and Meth. **B 164-165** (2000) 168.
[2] Y. Wada *et al.*, Nucl. Instr. and Meth. **B 204** (2003) 570.
[3] L. Weissman, D. Davies, P.A. Lofy and D.J. Morrissey, Nucl. Instr. and Meth., in press.
[4] D. J. Morrissey, B. M. Sherrill, M. Steiner, A. Stolz and I. Wiedenhoever, Nucl. Instr. and Meth. **B 204** (2003) 90.
[5] C. Scheidenberger*et al.*, Nucl. Instr. and Meth. **B 204** (2003) 119.
[6] L. Weissman, P.A. Lofy, D.A. Davies, D.J. Morrissey, P. Schury, S. Schwarz, T. Sun and G. Bollen, Proc. RNB6, editor G. Savard, Nucl. Phys. A, in press.
[7] J. F. Ziegler, computer code SRIM-2000, available from http://www.srim.org/SRIM.
[8] D. Bazin, O. Tarasov, M. Lewitowicz, O. Sorlin, Nucl. Instr. and Meth. **A 482** (2002) 314, available from http://groups.nscl.msu.edu/lise/lise.htm
[9] C. Scheidenberger and H. Geissel, Nucl. Instr. and Meth. **B135** 25 (1998) and http://www-aix.gsi.de/~scheid/ATIMA1.html
[10] H. Geissel, T. Schwab, P. Armbruster, J.P. Dufour, E. Hanelt, K.H. Schmidt, B. Sherrill, G. Munzenberg, Nucl. Instr. and Meth. **A 282** (1989) 247.
[11] http://www-linux.gsi.de/ weick/mocadi/
[12] http://www.phy.anl.gov/ria

TABLE I: Counting rate of ^{32}P, ^{33}S and ^{31}Si fragments as a function of the momentum slit gap. The obtained effective beam momentum spreads and rigidities (see text) are also shown.

Slits	nominal $\frac{\Delta P}{P}$	Effective $\frac{\Delta P}{P}$	Effective $B\rho$	Counting rate		
				^{32}P	^{33}S	^{31}Si
(mm)	(%)	(%)	(T·m)	(pps)	(pps)	(pps)
10	0.3	0.1	3.358	65	1.5	0.2
30	1	0.4	3.355	170	6	0.8
60	2	0.85	3.352	270	13	2

TABLE II: Fitting results for the obtained transmission profiles.

	nominal $\frac{\Delta P}{P} = 0.3\%$		nominal $\frac{\Delta P}{P} = 1\%$		nominal $\frac{\Delta P}{P} = 2\%$	
Fit	H		H		H	
parameter	0 Torr	825 Torr	0 Torr	825 Torr	0 Torr	825 Torr
a	1.02(1)	1.025(10)	1.04(2)	1.04(2)	1.05(2)	1.04(5)
b	3.149(1)	3.111(1)	3.125(2)	3.076(1)	3.081(2)	3.035(6)
k	0.0179(8)	0.0159(7)	0.0366(14)	0.0400(13)	0.0515(12)	0.0494(21)
Fit	M		M		M	
parameter	0 Torr	825 Torr	0 Torr	825 Torr	0 Torr	825 Torr
a	1.00(1)	0.99(1)	1.015(10)	1.01(1)	1.01(1)	1.02(1)
b	3.223(1)	3.185(2)	3.212(1)	3.170(1)	3.185(8)	3.145 (6)
k	0.0149(9)	0.0142(6)	0.0221(9)	0.0221(9)	0.0319(8)	0.0283(8)
b^M-b^H	0.075(2)	0.074(2)	0.087(2)	0.094(1)	0.104(8)	0.101(8)

TABLE III: Fitting results for the stopping profiles. The areas under the stopping profiles, S, are also shown. All values are given in millimeters, except the last two rows where the width of the stopping profile is given in mg/cm^2 and the equivalent length of He at 825 Torr pressure.

Fit	nominal $\frac{\Delta P}{P} = 0.3\%$		nominal $\frac{\Delta P}{P} = 1\%$		nominal $\frac{\Delta P}{P} = 2\%$	
parameter	H	M	H	M	H	M
x_c	3.132(2)	3.206(2)	3.095(5)	3.191(2)	3.069(10)	3.172(3)
y_c	0.51(2)	0.58(2)	0.31(3)	0.44(2)	0.20(4)	0.355(40)
w	0.029(1)	0.027(1)	0.061(2)	0.038(1)	0.078(3)	0.049(2)
S	0.037(1)	0.038(1)	0.047(4)	0.042(2)	0.039(7)	0.043(5)
w(mg/cm^2)	7.3(1)	6.6(1)	15.2(3)	9.3(2)	19.5(4)	12.3(3)
w(cm of He)	41	37	85	55	110	69
x_c^M-x_c^H	0.074(3)		0.096(6)		0.093(4)	

FIG. 1: General schematic view of the experimental setup.

FIG. 2: Typical identification plots : ΔE-E (a) and ΔE-TOF (b). The spectra were taken for the nominal momentum distribution of 2%, without gas and the degraders.

FIG. 3: The summary of measurements for the 0.3%, 1% and 2% nominal incident momentum distributions (0.1%, 0.4% and 0.85% effective distributions). For each case empty symbols correspond to the normalized data for the evacuated chamber and filled ones for the corresponding measurements taken at a gas pressure of P=825 Torr. To obtain the absolute rates the normalized data has to be multiplied by the counting rates from Table I. The solid lines correspond to the fits of the transmission profiles and the dotted lines represent the obtained stopping profiles.

FIG. 4: a-b. The residual energy spectra taken for the M- and H-wedges and 0.3%, 1% and 2% nominal incident momentum distributions (0.1%, 0.4% and 0.85% effective distributions). c-d. The corresponding energy spectra calculated with the LISE program [8] for the effective momentum distributions and beam rigidities.

FIG. 5: The calculated stopping profiles (thin lines) are compared to the experimental data (dotted lines) for the two wedges and the three values of the beam momentum spread. The calculations are done for the effective beam momentum distributions and rigidities (see text)

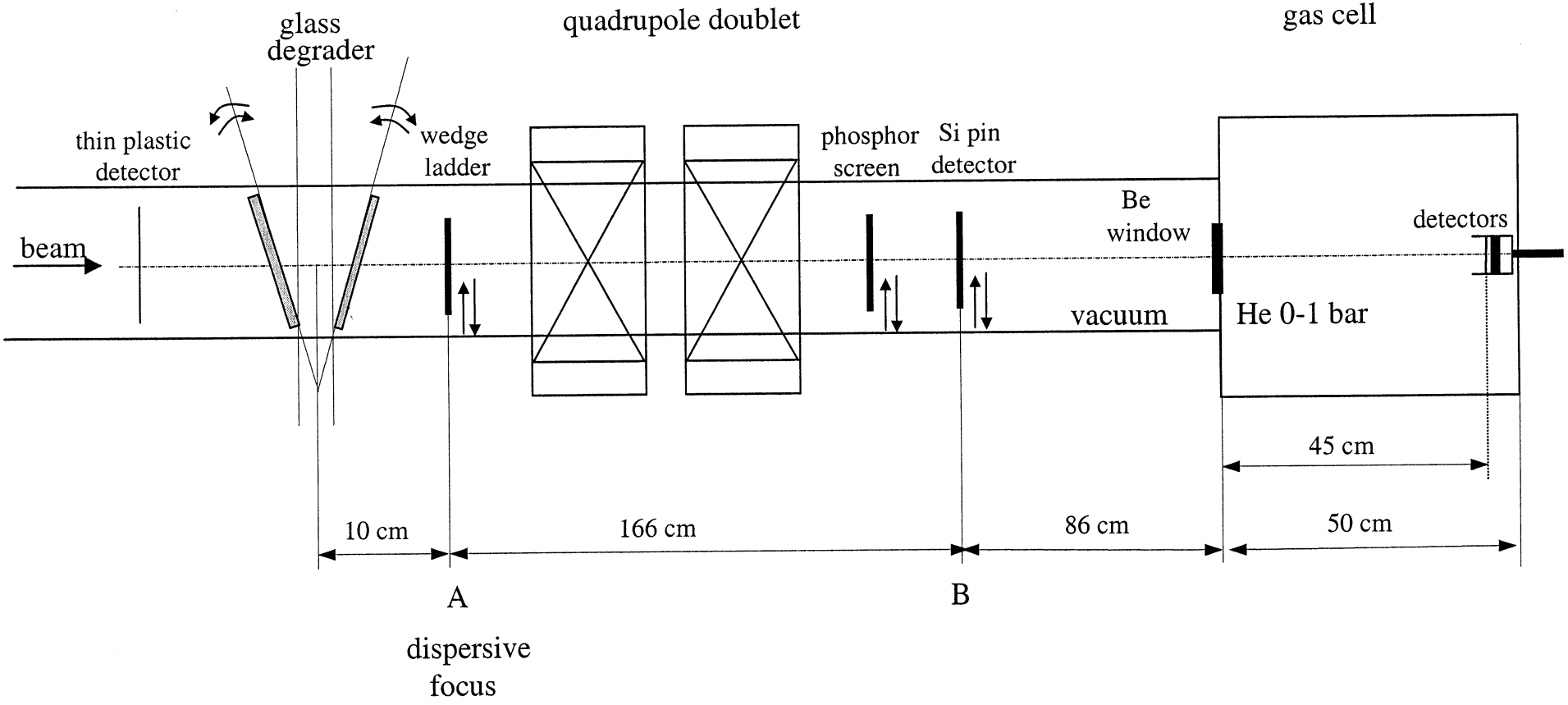
glass
degrader
quadrupole doublet
gas cell
thin plastic
detector
wedge
ladder
phosphor
screen
Si pin
detector
Be
window
detectors
beam
vacuum
He 0-1 bar
45 cm
10 cm
166 cm
86 cm
50 cm
A
B
dispersive
focus

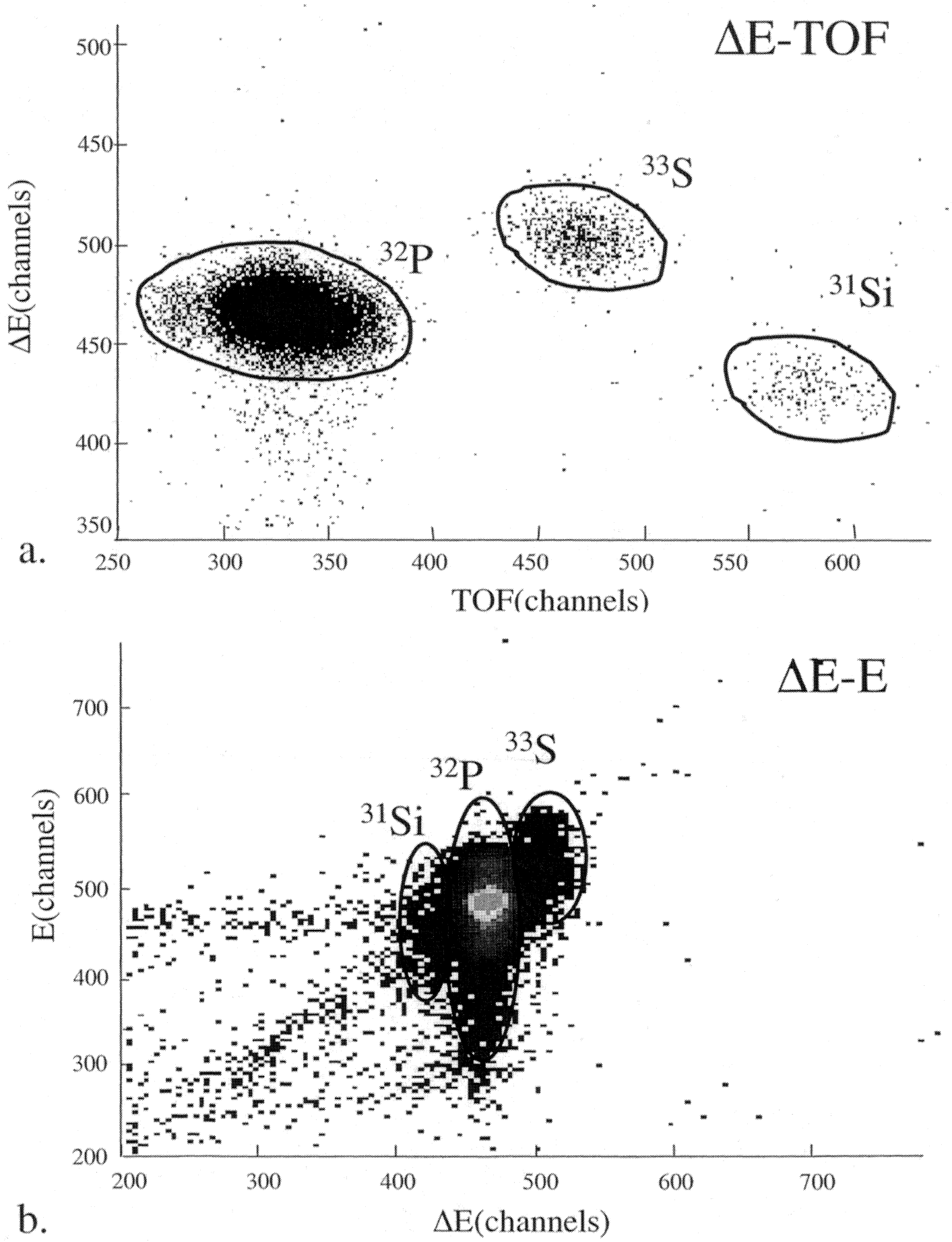
ΔE-TOF
33S
32P
31Si
ΔE(channels)
TOF(channels)
500
450
500
450
400
350
250
300
350
400
450
500
550
600
a.
ΔE-E
33S
32P
31Si
E(channels)
ΔE(channels)
700
600
500
400
300
200
200
300
400
500
600
700
b.

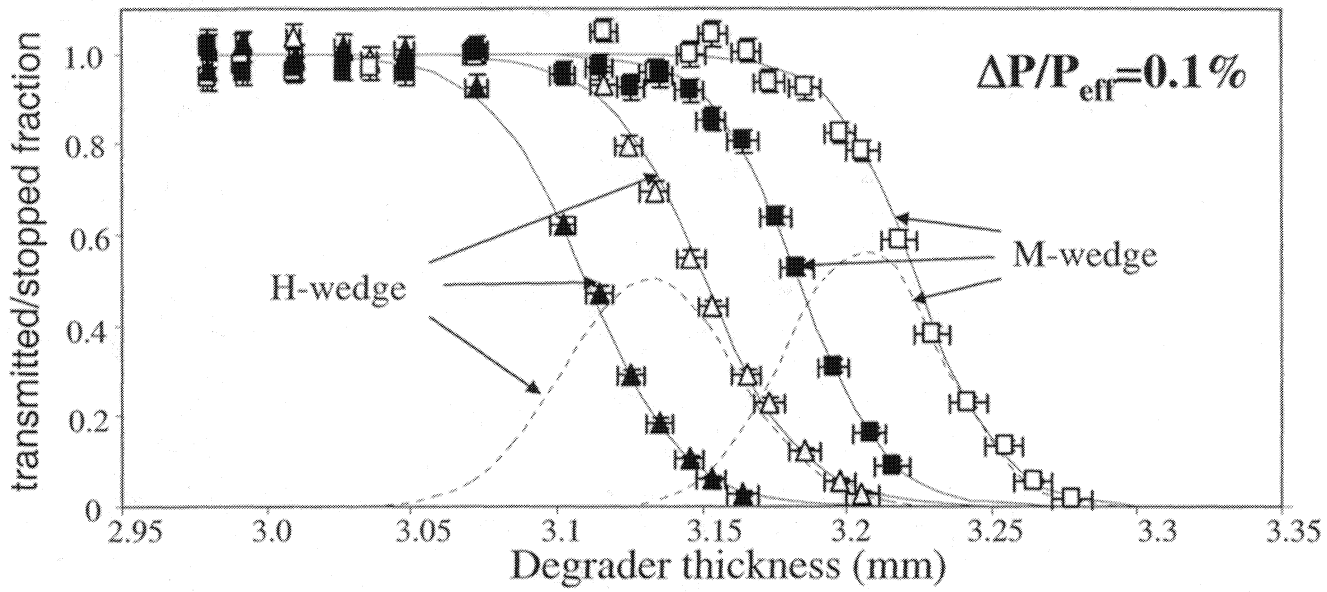
transmitted/stopped fraction
1.0
0.8
0.6
0.4
0.2
0
2.95
3.0
3.05
3.1
3.15
3.2
3.25
3.3
3.35
Degrader thickness (mm)
ΔP/P_eff=0.1%
H-wedge
M-wedge

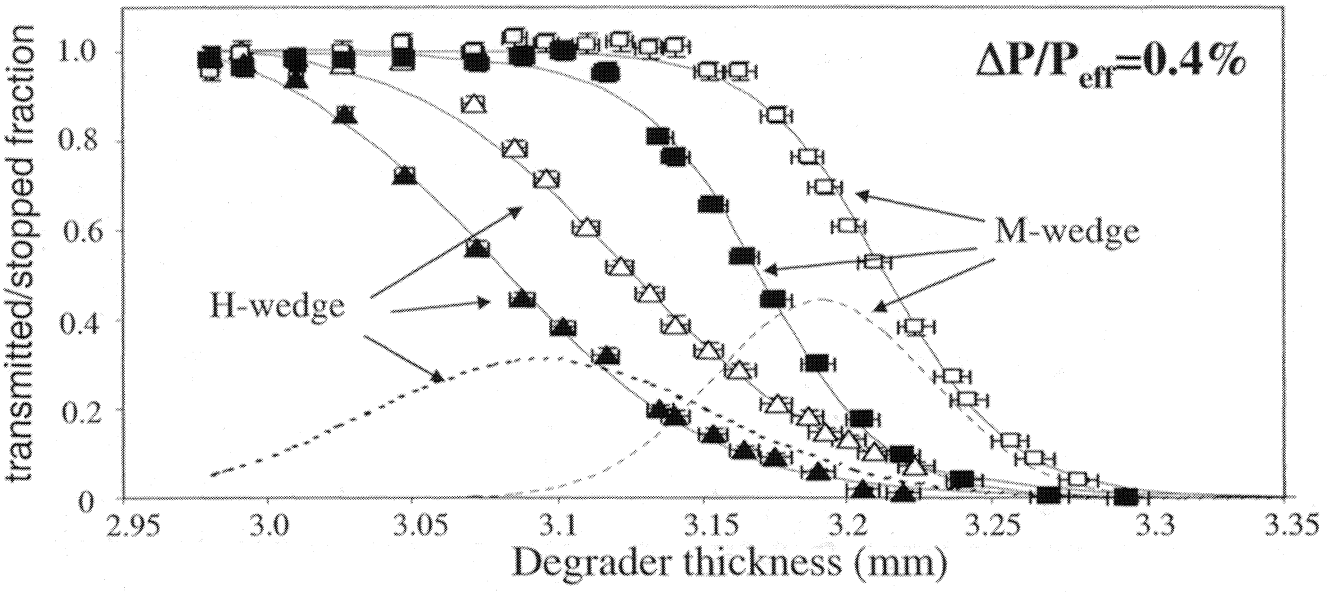
transmitted/stopped fraction
1.0
0.8
0.6
0.4
0.2
0
2.95
3.0
3.05
3.1
3.15
3.2
3.25
3.3
3.35
Degrader thickness (mm)
ΔP/P_eff=0.4%
H-wedge
M-wedge

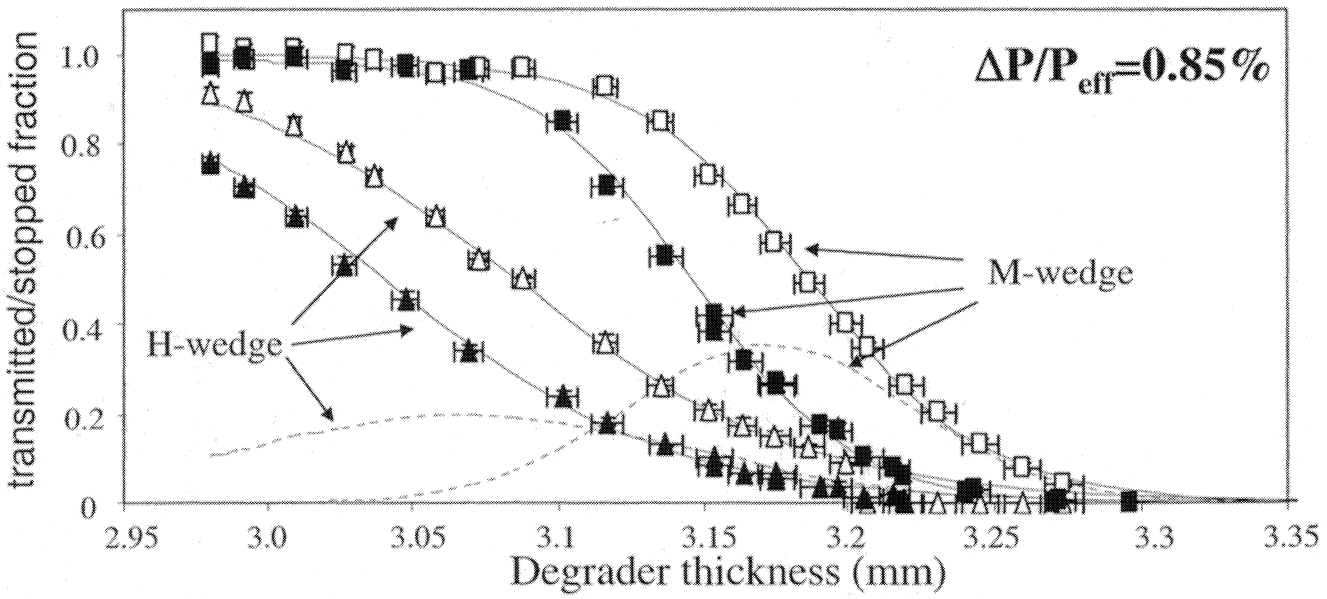
transmitted/stopped fraction
1.0
0.8
0.6
0.4
0.2
0
2.95
3.0
3.05
3.1
3.15
3.2
3.25
3.3
3.35
Degrader thickness (mm)
ΔP/P_eff=0.85%
H-wedge
M-wedge

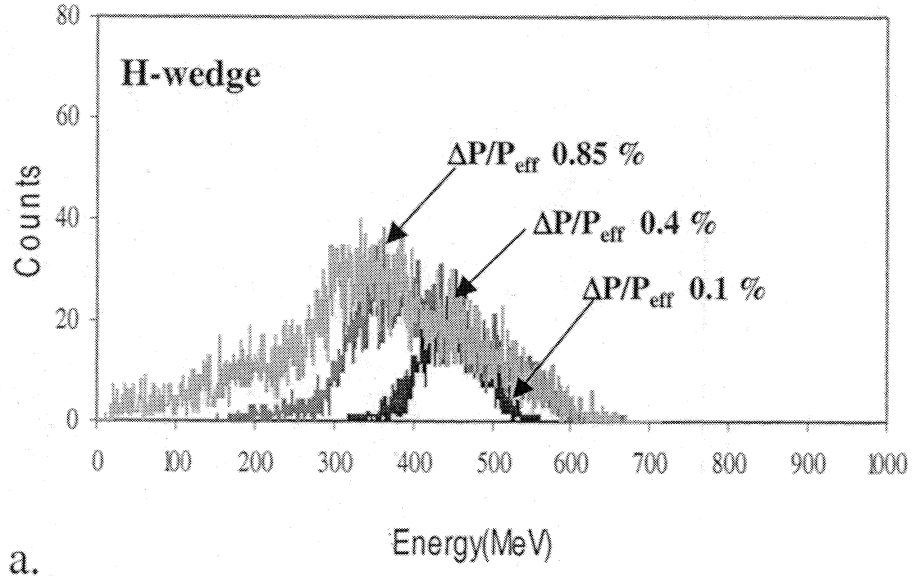
H-wedge
ΔP/P_eff 0.85 %
ΔP/P_eff 0.4 %
ΔP/P_eff 0.1 %
Counts
Energy(MeV)

a.

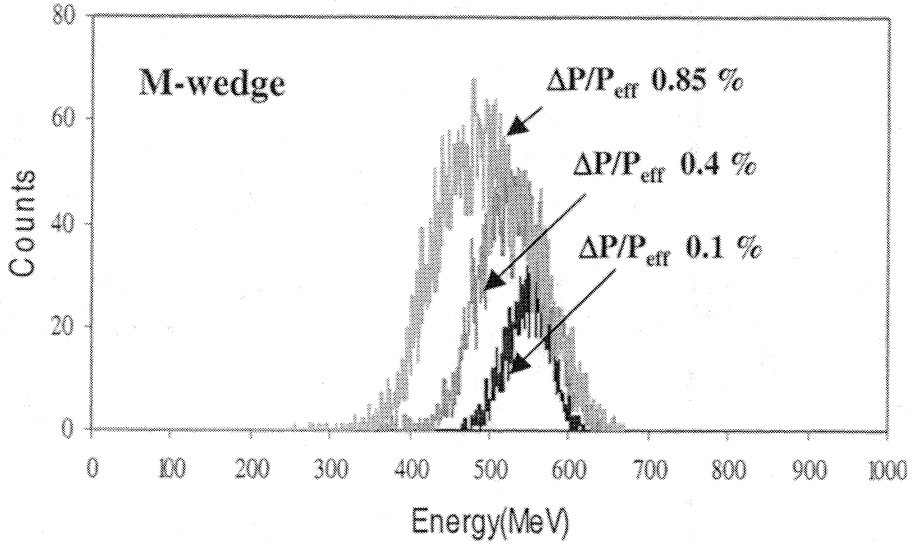
M-wedge
ΔP/P_eff 0.85 %
ΔP/P_eff 0.4 %
ΔP/P_eff 0.1 %
Counts
Energy(MeV)

b.

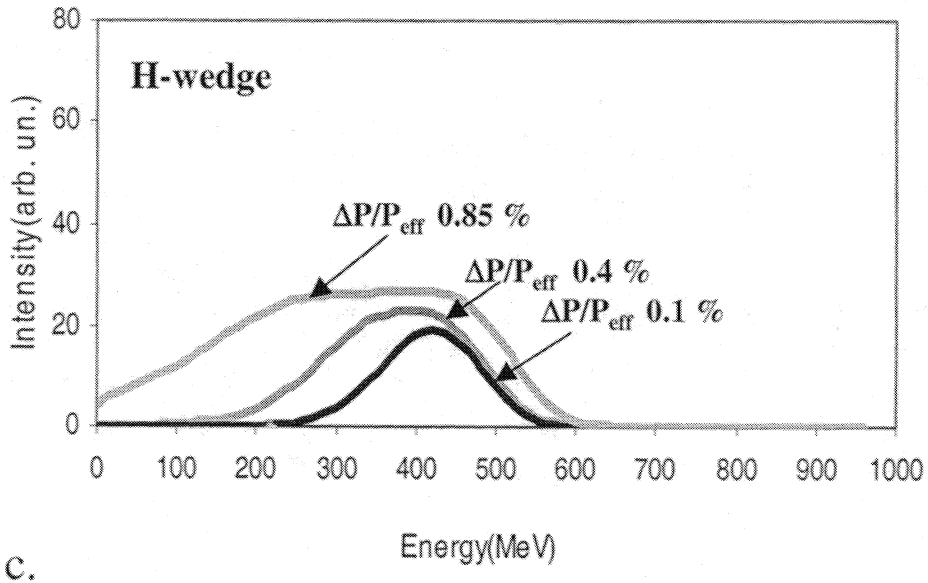
H-wedge
ΔP/P_eff 0.85 %
ΔP/P_eff 0.4 %
ΔP/P_eff 0.1 %
Intensity(arb. un.)
Energy(MeV)

c.

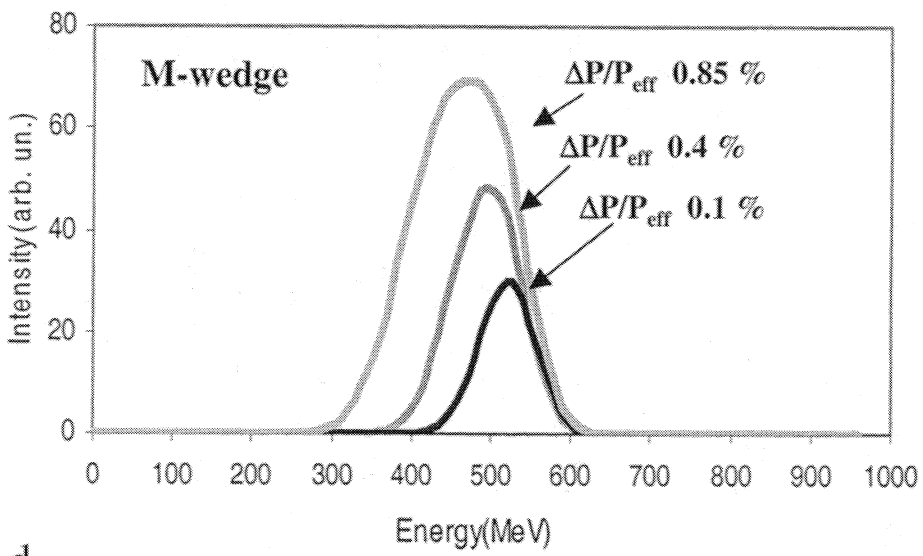
M-wedge
ΔP/P_eff 0.85 %
ΔP/P_eff 0.4 %
ΔP/P_eff 0.1 %
Intensity(arb. un.)
Energy(MeV)

d.

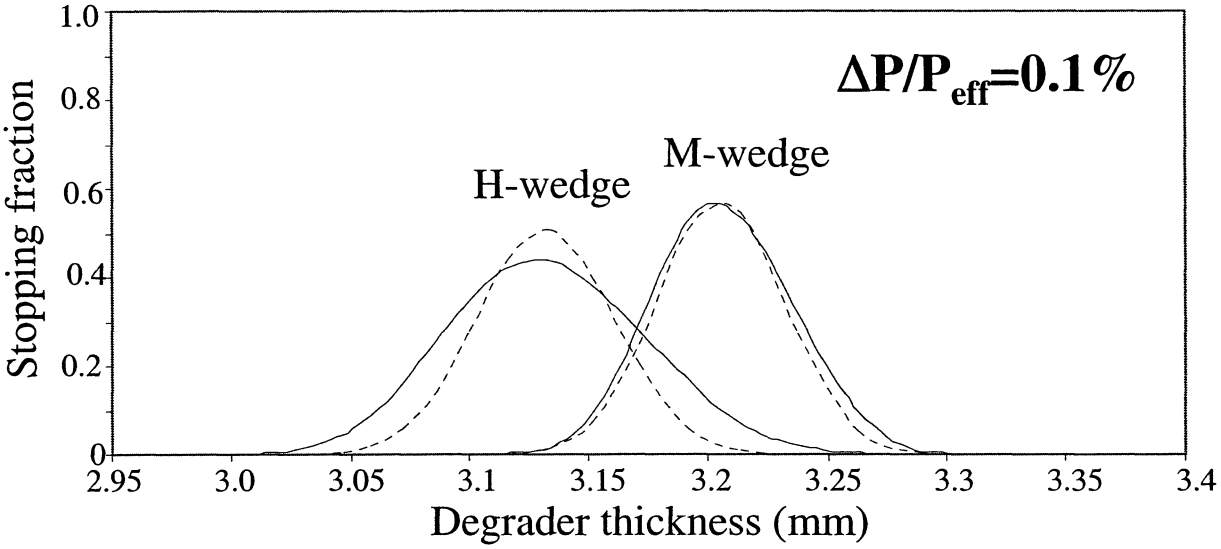
ΔP/P_eff=0.1%
M-wedge
H-wedge
Stopping fraction
1.0
0.8
0.6
0.4
0.2
0
2.95
3.0
3.05
3.1
3.15
3.2
3.25
3.3
3.35
3.4
Degrader thickness (mm)

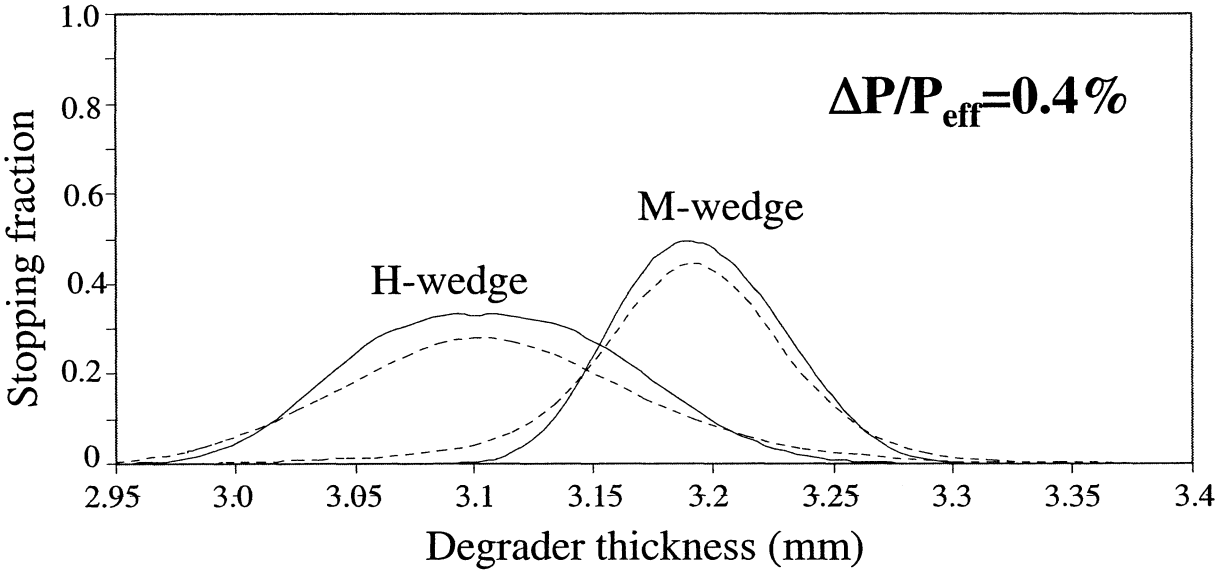
ΔP/P_eff=0.4%
M-wedge
H-wedge
Stopping fraction
1.0
0.8
0.6
0.4
0.2
0
2.95
3.0
3.05
3.1
3.15
3.2
3.25
3.3
3.35
3.4
Degrader thickness (mm)

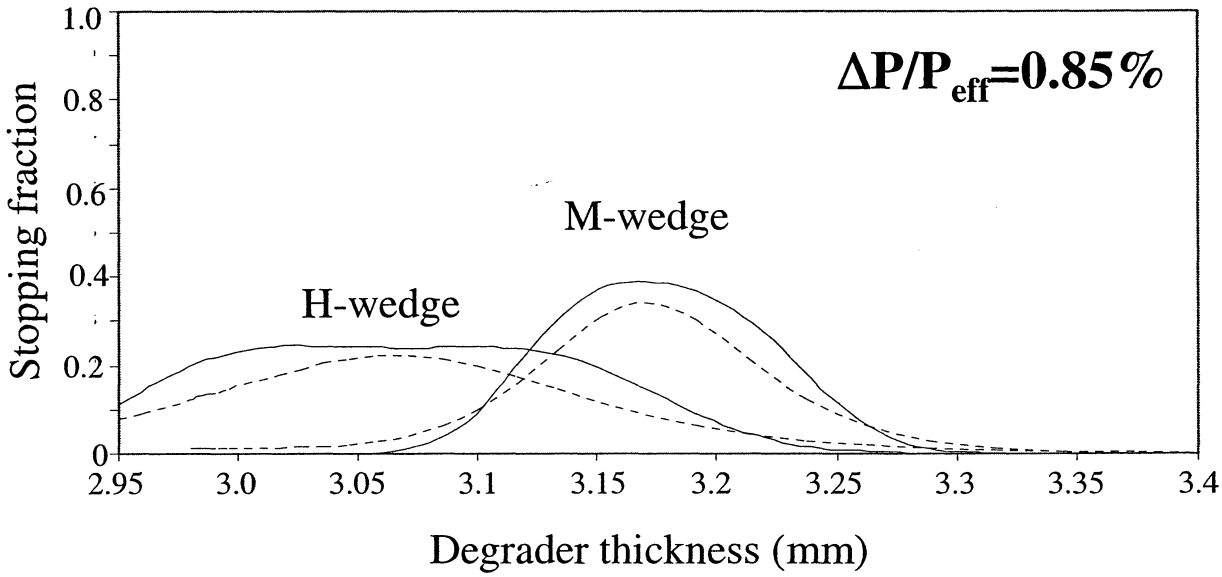
ΔP/P_eff=0.85%
M-wedge
H-wedge
Stopping fraction
1.0
0.8
0.6
0.4
0.2
0
2.95
3.0
3.05
3.1
3.15
3.2
3.25
3.3
3.35
3.4
Degrader thickness (mm)